ELSEVIER

Marine Geology 158 (1999) 147–160

MARINE GEOLOGY
INTERNATIONAL JOURNAL OF MARINE GEOLOGY, GEOCHEMISTRY AND GEOPHYSICS

www.elsevier.com/locate/margeo

Field observations of bedforms and sediment transport thresholds of fine sand under combined waves and currents

Michael Z. Li *, Carl L. Amos

Geological Survey of Canada (Atlantic), Bedford Institute of Oceanography, P.O. Box 1006, Dartmouth, NS B2Y 4A2, Canada

Received 28 May 1997; accepted 17 September 1998

Abstract

Seabed video images and S4 wave–current meter data, collected during the build-up of a moderate storm on the Scotian Shelf, are analysed for bedform development and sediment transport threshold of fine sand under combined waves and currents. As the storm built up, the following sequence of bedforms was observed: (1) relict wave-dominant ripples with worm tubes and animal tracks during the preceding fairweather period; (2) irregular, sinuous, asymmetrical current-dominant and intermediate wave–current ripples under bedload transport; (3) regular, nearly straight or sinuous asymmetrical to slightly asymmetrical wave-dominant ripples under saltation/suspension; (4) upper-plane bed under sheet-flow conditions; (5) small, crest-reversing, transitory ripples at the peak of the storm; and (6) large-scale lunate megaripples which developed when the storm decayed. These data also show that only single sets of asymmetrical intermediate wave–current ripples will form when waves and currents are co-linear. The development of the crest-reversing transitory ripples indicates a high-energy transition stage under quasi-sheet-flow conditions. A direct comparison of the skin-friction combined shear velocity and the critical shear velocities for bedload, suspension and sheet-flow transport under-estimated the onset of these sediment transport modes. As the presence of ripples causes the shear stress to increase from ripple trough to ripple crest, the ripple-enhanced skin-friction shear velocity must be used to determine properly the initiation of bedload transport. At high transport stages, the boundary layer dynamics is controlled mainly by the thickness of the bedload transport layer. Thus a transport-related bedload shear velocity, predicted based upon the sum of the grain roughness and bedload roughness, has to be compared against the conventional threshold criterion to properly define the onset of suspension and sheet-flow transport modes.

Keywords: continental shelf; combined waves and currents; ripple dynamics; sediment transport threshold

1. Introduction

With an increase in bed shear stress in natural flows, the following modes of sediment transport will be encountered: bedload, suspension, and sheet-flow transport. The threshold criteria for these transport modes need to be defined properly before sediment transport rates can be predicted. For wave-only conditions, several studies have indicated the applicability of the Shields parameter as the threshold for bedload transport (Komar and Miller, 1974; Madsen and Grant, 1975). Different threshold criteria have been proposed for sheet flow under waves

* Corresponding author. Tel.: +1 (902) 426-9459; Fax: +1 (902) 426-4104; E-mail: li@agc.bio.ns.ca

0025-3227/99/$ – see front matter
PII: S0025-3227(98)00166-2

(Manohar, 1955; Komar and Miller, 1975; Dingler and Inman, 1976; Nielsen, 1981), but no consensus has been reached. For the more complex case of combined waves and currents, studies on various transport thresholds are very limited (Hammond and Collins, 1979; Larsen et al., 1981; Kapdasli, 1990). These field and laboratory studies generally indicate the applicability of the Shields parameter for use under combined waves and currents, though Amos et al. (1988) propose that partitioned wave and current shear stresses can be used to approximately define the bedload threshold for fine sand under combined flows.

When transport modes change from bedload through suspension to sheet flow, various bedforms ranging from small ripples to upper-plane bed will occur. The correct prediction of bedform types and their dimensions directly controls the estimation of bed roughness and shear stress and the sand resuspension process (Smith, 1977; Grant and Madsen, 1982; Vincent et al., 1991; Li et al., 1996). Field and laboratory studies have shown that as the bed shear stress increases, wave ripples change directly into upper-plane bed for fine sand, while large-scale wave ripples can form as an intermediate step between small ripples and upper-plane bed over medium and coarse sands (Clifton, 1976; Allen, 1982; Harms et al., 1982). Bedforms generated under combined waves and currents are poorly understood. Amos et al. (1988) have studied ripple types and stability over fine sand under nearly orthogonal waves and currents on the Scotian Shelf. There are very few observations of large-scale ripples under combined waves and currents, although hummocky megaripples have been observed on continental shelves and in the nearshore (Swift et al., 1983; Greenwood and Sherman, 1986; Amos et al., 1996).

In an on-going field study of boundary layer dynamics and sediment transport processes on the Scotian Shelf (see Fig. 1), Li et al. (1997) collected hydrodynamics and seabed response data at a site of medium sand (Site 1 of Fig. 1). These data were used by Li et al. (1997) to study the interaction between waves and currents, the thresholds of various transport modes, and the applicability of different transport formulae under the combined-flow condition. Using that same data set, Li and Amos (1998) then evaluated the prediction of ripple geometry and bed roughness under combined waves and currents. The existing wave-ripple predictors were found not applicable to combined flows and a new empirical ripple predictor was thus proposed. Following the experiment at the medium-sand site, an instrumented tripod and a S4 wave–current meter were deployed in a deeper site (Site 2 of Fig. 1) over fine sand sediment. The complete process of a storm build-up was recorded; during this, various types of bedforms and different transport modes were observed. This paper will present the wave–current dynamics and seabed response data collected from this fine-sand site. The results presented in this paper will be a natural follow up of our previous work over medium sand sediment, and will extend the findings of sediment transport thresholds over medium sand to fine sand sediment. Different from the previous data set, the video camera used in this deployment recorded the continuous processes of particle entrainment, ripple migration/oscillation, and the complete wash-out of ripples under sheet-flow condition. This has enabled us to study the morphology and dynamic transition of various bedform types (bedform dynamics) which was not done in our previous papers.

2. Data collection and analysis

2.1. Regional setting

Sable Island Bank is located about 180 km off Nova Scotia (Fig. 1), on the east coast of Canada. The bank is underlain by approximately 20 m of well-sorted Holocene sand, moulded into a series of shoreface-connected sand ridges. Tidal currents are semidiurnal and rotate 360º in a clockwise direction over a tidal cycle. Peak tidal flows reach 0.35 m/s near the seabed and are strongly anisotropic (northeast to southwest). Waves originate generally from the south and southwest due to the sheltering by Sable Island to the north. In the study region, peak significant wave heights and mean wave periods can reach 6–8 m and 10–13 s, respectively, during the winter months (December to February). During the summer, significant wave heights are less than 2 m. More details of the physical oceanography and surficial geology can be found in Mobil Oil Canada Ltd. (1983) and Amos et al. (1988).

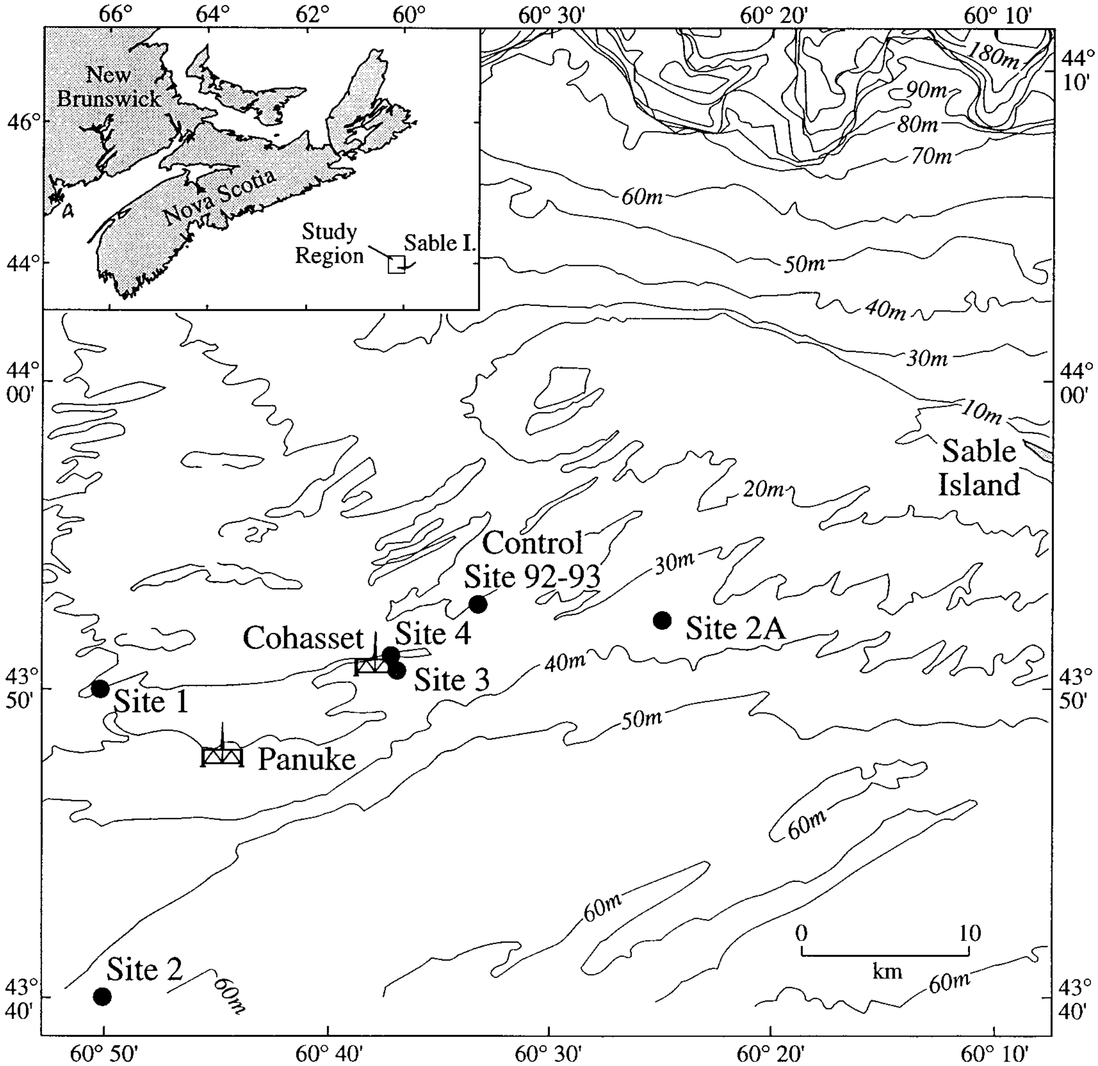

Fig. 1. The location map showing the study region on Sable Island Bank, Scotian Shelf, and the sites of field experiments.

2.2. The study site and instrumentation

An instrumented tripod and a S4 wave–current meter (InterOcean Systems Inc.) were deployed at Site 2 (43°39′58″N, 60°49′55″W) in the study region (Fig. 1), from February 27 to March 25 of 1993, to collect data on waves, currents, suspended sediment concentrations and seabed responses. The water depth at the deployment site was 56 m and a van Veen grab sample showed the bottom sediment to be well-sorted fine quartz sand, with a median grain size (D) of 0.20 mm. The tripod was equipped with a pressure transducer located at 1.6 m above the bottom (ab), six Optical Backscatter Sensors (OBS, Downing, 1983) at heights ranging from 0.1 to 1.6 m ab, and a Sony 101 video camera with a scaled shadow bar for ripple geometry and migration measurements. Data were logged on an Onset TattleTale Model 6 microcomputer, which was programmed to sample continuously at a frequency of 0.5 Hz. The video camera recorded the seabed condition for 10 s every hour.

The InterOcean S4 wave–current meter is a self-contained, spherical, electromagnetic sensor that measures water depth, waves, current magnitude and direction. Data are stored internally in a 1 Mbyte solid-state memory. The S4 meter was supported by a $1.5 \times 1.5 \times 1.5$ m stainless-steel weighted base with the electrodes situated 0.5 m ab. The S4 meter burst-sampled data for a duration of 10 min every 2 h at a frequency of 1 Hz and was synchronized with the video camera. The S4 meter was calibrated in a towing-tank and the average error was about $\pm 4\%$ for a velocity range from 0.03 to 1.5 m/s.

2.3. Data analysis

Each data burst recorded by the S4 meter was averaged to obtain the mean water depth (h), the mean current speed at 50 cm ab (u_{50}) and its direction (C_{dir}). The depth time-series was de-meaned and used to compute the wave spectral density. The spectral-peak wave period (T_p) was estimated from the peak of this spectrum and the significant wave height (H_s) was obtained from $4M_0^{0.5}$ where M_0 (in m^2) is the first moment of the wave spectral density. For each velocity time-series, the mean values of the x (east–west) and y (north–south) components were removed from the instantaneous speed to obtain the wave orbital velocities. A least-square regression line was fitted to the scatter plot of the x and y components of the wave orbital velocities to determine the mean wave direction (W_{dir}). The burst-averaged h, u_{50}, C_{dir}, H_s, T_p, W_{dir} and median grain size D (in form of grain-size roughness height $2.5D$) were used in the combined-flow bottom boundary layer (bbl) model of Grant and Madsen (1986, GM86 hereafter) to compute various shear velocities which were then compared with the observed seabed responses to evaluate bedform transition and threshold shear stresses for various transport modes.

Each of the 10 s seabed video records was analysed for ripple types and bed state classification. Bedload transport was determined by visual detection of near-bed sand particle movements at the ripple crests and/or ripple pattern change between the two consecutive records. The presence of ‘sand clouds’ in the water column, together with general deterioration of image clarity, marks the initiation of sediment suspension. The combination of sand suspension and complete local wash-out of ripples indicates the upper-plane bed sheet-flow conditions. The scaled shadow bar on the tripod was bent from its original setting during the deployment process and thus ripple heights could not be obtained for this data set. However, the scales on the shadow bar before it was bent were used to estimate ripple wavelengths.

3. Results

3.1. General description of data

The S4 meter recorded data from February 27 to March 25 for a total of 323 bursts. Time-series (in Julian days, JD) of burst-averaged depth h, mean current speed u_{50}, significant wave height H_s and spectral-peak wave period T_p are plotted in Fig. 2 to provide an overview of the data. The depth time-series (Fig. 2a) clearly shows the semi-diurnal tidal cycles. The maximum tidal range during spring tides reached about 1.5 m and the minimum range was only about 0.5 m during neap tides. The mean current speed u_{50}, as shown in Fig. 2b, ranged from less than 0.1 m/s during neaps to about 0.25 m/s during springs or storms. The time-series plots of H_s and T_p (Fig. 2c,d) show one major storm (around Julian Day 74) and four smaller wave events. Significant wave height and wave period reached about 7 m and 16 s during the major event, and were 1–3 m and less than 13 s, respectively, during the four smaller events.

The OBS sensors on the tripod unfortunately did not function during this deployment, while the video camera collected only 120 ten-second records. Nevertheless, these video records were correlated with the S4 meter data from 2:00 of JD 58 to 4:00 of JD 60 and provided complete information on waves, currents and seabed responses during the build-up of the first storm shown in Fig. 2c. These correlated video and S4 meter data were analysed further for bedform development and sediment transport threshold. The time-series of the burst-averaged u_{50} and H_s of the S4 data that overlapped with the video data are plotted in the upper two panels in Fig. 3, and the observed seabed responses were plotted in the bottom panel of the figure in which the following numbers have been assigned to the observed bed states of increasing energy: 1 = no motion, 2 =

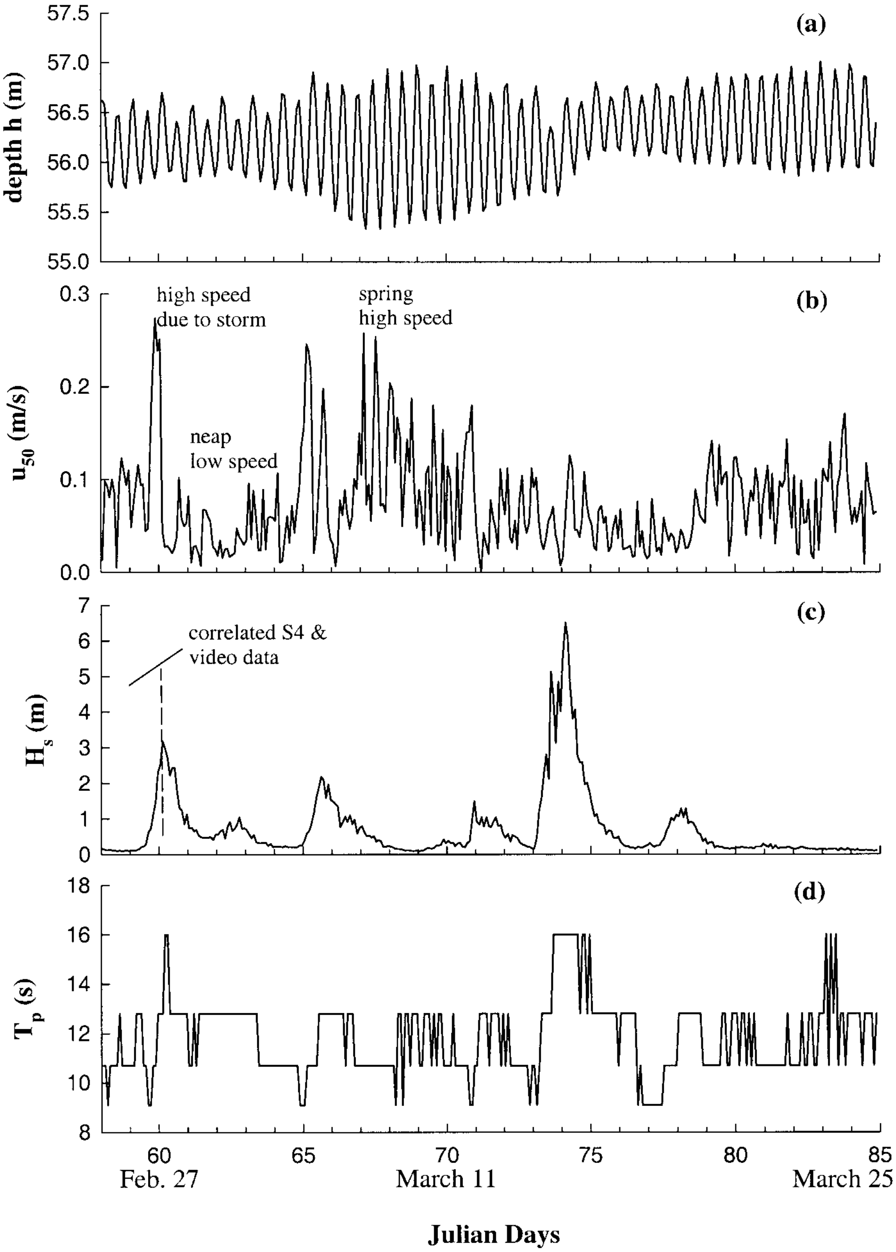

Fig. 2. Time-series plots of the S4 meter data: (a) burst-averaged mean water depth h (m); (b) mean current speed at 50 cm above the bottom u_{50} (m/s); (c) significant wave height H_s (m); (d) spectral-peak wave period T_p (s).

bedload, 3 = suspension, and 4 = sheet flow. Six representative bedform types observed during this storm build-up were digitized from the video tape and are given in Fig. 4. The correlated wave/current and seabed response data, shown in Fig. 3, can be divided into two parts. The first part was a fairweather period before hour 39 and the second was a period of storm build-up from hour 39 to hour 51. During the fairweather period, the mean current speed u_{50} was about 0.1 m/s and the significant wave height H_s was

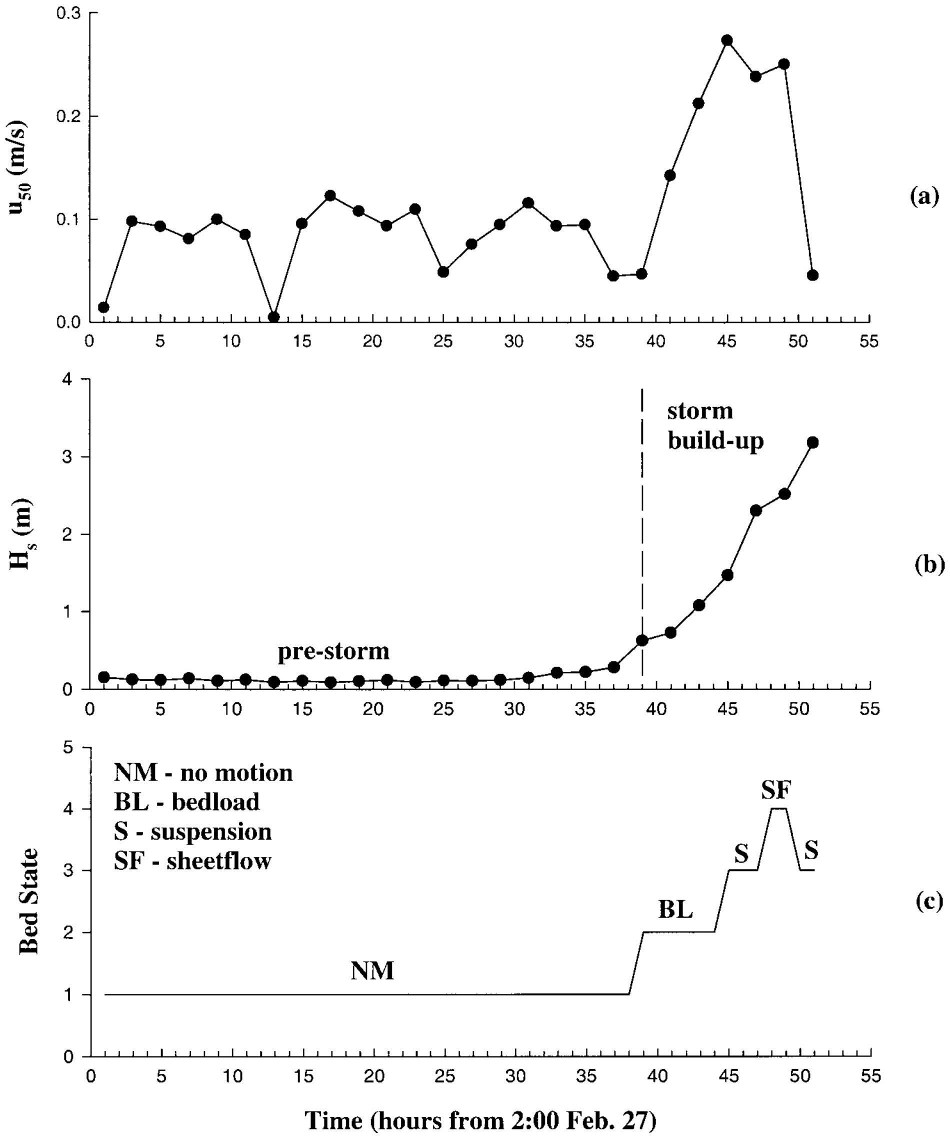

Fig. 3. Time-series plots of the correlated S4 meter and video camera data: burst-averaged (a) mean current speed u_{50} (m/s); (b) significant wave height H_s (m); (c) observed bed state: *1* = no motion, *2* = bedload, *3* = suspension, *4* = sheet flow.

less than 0.3 m. The seabed was covered with relict ripples and no sediment movement (NM) was observed (Fig. 3c). The second part of the data shows that as the storm quickly built up, H_s increased rapidly from 0.3 m to 3.2 m and u_{50} reached about 0.25 m/s. Corresponding to the storm build-up, a sequence of bedload transport (BL), sand suspension (S) and upper-plane bed sheet-flow transport (SF) was observed in the videos (Fig. 3c).

3.2. Bedform dynamics

Of the correlated video and S4 meter data, the video images of the first 20 bursts showed similar relict ripples, with no sediment transport. Various transport modes and bedforms only occurred in the last six bursts. Thus the last eleven bursts have been selected for further analysis of the boundary layer dynamics, bedform transition and the thresholds for

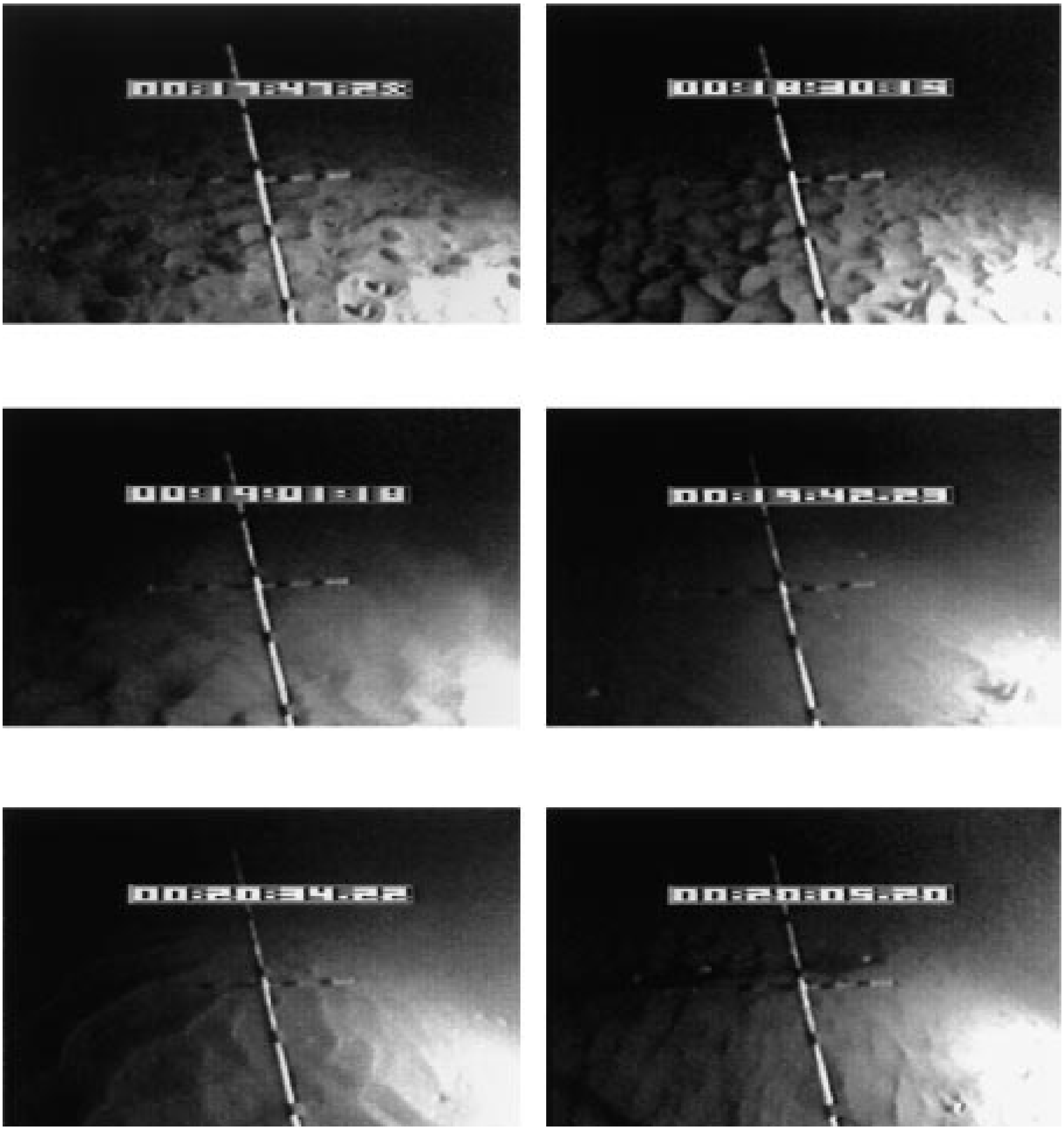

Fig. 4. Representative bedform types observed during the storm build-up process: relict ripples (no motion) in image 17:47; bedload transport in 18:30; suspension transport in 19:01; upper-plane bed sheet flow in 19:42; sand suspension over crest-reversing transitory ripples in 20:34; lunate megaripples in 20:05. The numbers were put on these photos during processing only for reference purpose. The marks on the scale bars represent horizontal distances of 10 cm and 5 cm, respectively, though the bar was bent during deployment.

various sediment transport modes. Table 1 lists the following: burst number (BT, hours from 2:00 of JD 58), (Julian) day:hour, burst-averaged water depth h, mean current speed u_{50}, direction of the mean current C_{dir}, significant wave height H_s, spectral-peak wave period T_p, and wave-propagation direction W_{dir}. The

Table 1
Measured wave and current data of the last 11 bursts of the correlated S4 and video data

BT (h)	Day:Hour	h (m)	u_{50} (m/s)	C_{dir} (°)	H_s (m)	T_p (s)	W_{dir} (°)
31	59:08	56.0	0.116	218	0.15	12.8	314
33	59:10	55.8	0.094	261	0.21	12.8	338
35	59:12	56.0	0.095	304	0.22	10.7	313
37	59:14	56.3	0.045	303	0.28	10.7	301
39	59:16	56.5	0.047	258	0.62	9.1	301
41	59:18	56.3	0.143	275	0.73	9.1	299
43	59:20	56.0	0.213	276	1.08	10.7	305
45	59:22	55.8	0.274	294	1.47	10.7	301
47	60:00	56.0	0.239	315	2.31	12.8	304
49	60:02	56.5	0.251	334	2.52	12.8	320
51	60:04	56.7	0.046	314	3.18	12.8	325

Mean water depth, h; mean current speed at 50 cm ab, u_{50}, and its direction, C_{dir}; significant wave height, H_s; spectral-peak wave period, T_p; mean wave direction, W_{dir}. The burst number (BT, hours from 2:00 Julian Day 58) and Julian Day:Hour are also given.

wave and current parameters presented in Table 1 were used in the combined-flow bbl model of Grant and Madsen (1986) to predict various boundary layer parameters. Grain size roughness alone was first used in the GM86 model to predict skin-friction wave (u_{*ws}), current (u_{*cs}) and combined (u_{*cws}) shear velocities. The mean current speed u_{50}, the predicted near-bed maximum wave orbital velocity u_b, the acute angles between waves and currents ϕ_{cw}, and the skin-friction combined shear velocity u_{*cws} are given in Table 2, together with brief summaries of the observed bedforms and transport modes in each burst. Since the video camera recorded seabed conditions every hour and the S4 meter recorded only one burst of data every two hours, there are two 10 s video records associated with each burst (BT) of the S4 data in Table 2.

From Julian Day 58 hour 02 to Julian Day 59 hour 16 (hours 0 to 39 in Fig. 3), the observed mean current u_{50} was generally less than 0.1 m/s and the significant wave height H_s less than 0.6 m. During this fairweather period, the video records show that the seabed was covered with relict cross-ripples with worm tubes, benthos tracks and abundant sand dollars (photo 17:47 in Fig. 4). The average wavelength of these ripples was 5–7 cm. No transport was observed for this period. According to Amos et al. (1988) and Li et al. (1997), these ripples are defined as relict wave-dominant ripples. Two hours later (hour 41 in Fig. 3 and BT 41 in Table 1), u_{50} and H_s had increased to 0.14 m/s and 0.73 m, respectively. Ripple pattern changes, shown by the consecutive video records from hours 39 and 41, indicate that

Table 2
Observed bedforms and transport modes of the selected bursts

BT (h)	u_{50} (m/s)	u_b (m/s)	ϕ_{cw} (°)	u_{*cws} (cm/s)	u_{*cwe} (cm/s)	u_{*cwb} (cm/s)	Observed bedforms and bed states
31	0.116	0.017	83	0.48	0.81	0.48	no motion; relict wave-dominant ripples with animal tracks and worm tubes
33	0.094	0.024	76	0.45	0.76	0.45	same as above
35	0.095	0.018	9	0.50	0.84	0.50	same as above
37	0.045	0.022	2	0.35	0.60	0.35	same as above
39	0.047	0.026	43	0.38	0.64	0.38	same as above
41	0.143	0.031	25	0.76	1.29	0.76	bedload; irregular, sinuous, asymmetrical ripples with bifurcation; $\lambda \approx$ 5–7 cm
43	0.213	0.085	29	1.34	2.15	1.63	bedload; irregular, asymmetrical to slightly asymmetrical ripples with bifurcation; straight, sinuous and linguoid ripples co-exist; $\lambda \approx$ 8 cm
45	0.274	0.116	7	1.79	2.81	2.80	strong suspension; nearly regular, straight and slightly sinuous, asymmetric or slightly asymmetrical ripples with bifurcation, $\lambda \approx$ 10 cm
47	0.239	0.263	10	2.50	2.64	4.63	strong to medium suspension; regular, nearly straight and sinuous asymmetrical ripples with bifurcation; $\lambda \approx$ 10 cm
49	0.251	0.284	15	2.65	2.65	5.02	sheet flow with medium–strong suspension; small, asymmetrical, crest-reversing transitory ripples with $\lambda \approx$ 8–9 cm
51	0.046	0.357	11	2.45	2.53	4.75	moderate suspension; lunate megaripple ($\lambda \approx$ 0.8 m) changing into small, asymmetrical, crest-reversing transitory ripples ($\lambda \approx$ 8 cm)

BT, hours from 2:00 of Julian Day 58. Also listed are mean velocity u_{50}; near-bed maximum wave orbital velocity, u_b; the acute angle between waves and currents, ϕ_{cw}; and various predicted shear velocities (see text for definitions).

bedload transport had occurred. The bedforms were irregular, sinuous, asymmetrical ripples with bifurcations. The ripple wavelengths ranged from 5 to 7 cm. At hour 43 (BT 43 of Table 1), u_{50} and H_s increased further to 0.21 m/s and 1.08 m, respectively. The video records of this burst (photo 18:30 in Fig. 4) show that the ripple pattern had changed and that motions of rolling/saltating of sand grains were observed at the ripple crests. These suggest bedload transport mode. Sinuous, linguoid and nearly straight ripples with bifurcations co-existed in this burst. The sinuous ripples were asymmetrical and the straight ripples were slightly asymmetrical. The average ripple wavelength was around 8 cm. The mean current reached a peak value of 0.27 m/s and the significant wave height increased to 1.47 m at hour 45 (Fig. 3 and BT 45 of Table 1). The video records from this burst (photo 19:01 of Fig. 4) show sand clouds in the water column, indicating transport in suspension mode. Seabed was covered by nearly regular, straight or slightly sinuous ripples with bifurcations. These ripples were asymmetrical or slightly asymmetrical. The average ripple wavelength was about 10 cm. By hour 47 (BT 47 in Tables 1 and 2), u_{50} had reduced slightly to 0.24 m/s and H_s had increased to 2.31 m. Strong suspension was observed over regular, nearly straight to sinuous, asymmetrical ripples with an average ripple wavelength of around 10 cm.

The strongest combination of waves and currents during this deployment occurred at hour 49 (Fig. 3 and BT 49 of Table 1), in which the mean current was 0.25 m/s and H_s further increased to 2.52 m. The video record of the first hour (photo 19:42 in Fig. 4) shows that local ripples were washed out completely and upper-plane bed sheet-flow conditions prevailed. Strong suspension was observed. In the second hour of the burst (photo 20:34 in Fig. 4), the suspension level had decreased. Continuous, nearly straight, highly asymmetrical small ripples were observed; their average wavelengths were around 8–9 cm. These small ripples tend to first develop at the end of the one-way wave oscillation. They will reverse their migration direction as the wave reverses, and are then washed out temporarily to change into sheet flow at the peak of the wave oscillation. In the last burst (hour 51 in Fig. 3 and BT 51 of Table 1), H_s increased to 3.18 m but the mean current dropped significantly to 0.05 m/s. The video record from the first hour of the burst (photo 20:05 in Fig. 4) shows moderate suspension over a lunate megaripple (*note the crest of the lunate megaripple running just above and roughly parallel with the small cross-bar and turning upward abruptly at its right end*). The wavelength of the lunate megaripple was estimated to be about 80 cm. In the second hour of the burst, the lunate megaripple was replaced by small crest-reversing, transitory ripples.

Amos et al. (1988) also studied combined-flow ripple formation on Sable Island Bank and defined six types of ripples based on ripple geometry and distribution patterns. Using their data set, they concluded that wave and current ripples co-existed, with their relative magnitudes dependent upon the relative strength of waves and currents, and that intermediate ripple types due to the combined influence of waves and currents were not seen. These authors stated also that these findings were only valid for nearly orthogonal waves and currents, and that ripple patterns generated under co-linear waves and currents were unknown. The waves and currents of this study were separated by small angles (7° to 29°) for the selected bursts 41 to 47 (Table 2). The video records of these bursts (photos 18:30 and 19:01 in Fig. 4) showed that only intermediate asymmetrical wave–current ripples occurred and that co-existing wave ripple and current ripple sets were not seen. These observations appear to suggest that, if waves and currents are parallel or form small angles, combined wave–current ripples intermediate between pure wave and current ripples will form, and that if waves and currents are orthogonal or form large angles, independent symmetrical wave ripples and asymmetrical current ripples will co-exist to form a honeycomb (or cross-ripple) pattern. Similar findings were also obtained in recent wave flume and wave–current basin experiments on fine-sand transport (van Rijn et al., 1993; van Rijn and Havinga, 1995). It is common for researchers to use the asymmetrical profile, among other ripple characteristics, to distinguish current or current-dominant ripples from wave or wave-dominant ripples under combined-flow conditions (Amos et al., 1988; Li and Amos, 1998). The findings from this and previous studies on ripples under co-linear waves and currents (Harms et al., 1982; van Rijn et al., 1993; van Rijn and Havinga, 1995) indicate that asymmetry of ripple profiles alone cannot be used to determine if ripples are current-dominant or wave-dominant. Other properties have to be considered to discriminate between these two types of ripples. Our observation suggests that the intermediate wave–current asymmetrical ripples are generally more regular and straighter with rounded crests, while asymmetrical current or current-dominant ripples under orthogonal waves and currents are more irregular, curved with sharp crests and tabular slip faces. Asymmetry and ripple steepness (height over wavelength) of wave–current ripples are intermediate between pure wave ripples and current ripples. The occurrence of zig-zag bifurcations is also an important distinguishing characteristic of the intermediate wave–current ripples.

The crest-reversing, asymmetrical small ripples, observed in burst 49, are defined as crest-reversing transitory ripples according to Harms et al. (1982). Their occurrence indicates a quasi-sheet-flow condition as a transition from suspension to upper-plane bed sheet-flow conditions or vice versa. The transitory ripples were also observed to form during the transition from sheet flow to lunate megaripples in burst 51. The formation of these ripples is due to the oscillatory motion of the combined flow, the near sheet-flow energetic condition and long wave periods at this stage of the storm. The asymmetrical profile, regular and long-crestal form of these transitory ripples, as observed from instantaneous seabed photos, are difficult to differentiate from lower-regime straight current ripples. However, the former represent wave-dominant, high-energy conditions. The small heights of these transitory ripples, together with their associated high-energy flow dynamics, should be used as diagnostic features to avoid possible mis-classification.

3.3. Thresholds of various sediment transport modes

In theories and numerical models of sediment transport, it is conventional to use the skin-friction shear stress or shear velocity to determine the threshold conditions for various sediment transport modes, i.e. bedload, suspension and sheet flow. Observed sediment transport modes and the skin-friction shear velocities $u_{*\mathrm{cws}}$ (predicted by the GM86 model using grain roughness only) for the listed bursts in Table 2 are plotted in Fig. 5 (as circles) to evaluate the thresholds of various transport modes for fine sand under combined waves and currents. The three dashed lines in Fig. 5b represent, from bottom to top, the critical shear velocities for bedload ($u_{*\mathrm{cr}} = 1.3$ cm/s), suspension ($u_{*\mathrm{crs}} = 2.0$ cm/s) and sheet flow ($u_{*\mathrm{up}} = 4.9$ cm/s). $u_{*\mathrm{cr}}$ was derived from the Yalin curve given by Miller et al. (1977) and $u_{*\mathrm{crs}}$ is obtained from Bagnold (1956), who proposed that the sand suspension will occur when shear velocity is roughly equal to the grain settling velocity w_{s}. $u_{*\mathrm{up}}$ is calculated from Komar and Miller (1975):

$$\theta_{\mathrm{up}} = 0.413 D^{-0.396} \tag{1}$$

where $\theta_{\mathrm{up}} = \rho u_{*\mathrm{up}}^2 / (\rho_{\mathrm{s}} - \rho) g D$ is the critical Shields parameter for sheet flow, g is the acceleration due to gravity, ρ and ρ_{s} are fluid and grain densities, respectively. D in Eq. 1 is in mm. Fig. 5 clearly shows the discrepancies between the observed transport modes and their established critical shear velocities, when $u_{*\mathrm{cws}}$ is used. Bedload transport was observed to start in burst 41 (Fig. 5a), but the skin-friction combined shear velocity $u_{*\mathrm{cws}}$ was only 0.76 cm/s; it is significantly lower than the required value of $u_{*\mathrm{cr}} = 1.3$ cm/s (Fig. 5b). Suspension was first observed in burst 45, yet the predicted $u_{*\mathrm{cws}}$ for this burst was only 1.79 cm/s; this is again below the critical shear velocity of $u_{*\mathrm{crs}} = 2.0$ cm/s for suspension. Similarly, sheet flow was observed in burst 49 (Fig. 5a) and the corresponding $u_{*\mathrm{cws}}$ of this burst was only 2.65 cm/s; once again, this is much below the required critical shear velocity of $u_{*\mathrm{up}} = 4.9$ cm/s for sheet flow (the upper dashed line in Fig. 5b).

In an earlier field study on boundary layer dynamics and sediment transport over *medium sand* in the same Sable Island Bank area, Li et al. (1997) also found similar discrepancies between $u_{*\mathrm{cws}}$ and various observed transport modes. Further, Li et al. argued that when the seabed is rippled, the shear stress will increase from ripple trough to crest. Hence, the enhanced shear velocity at the ripple crest, $u_{*\mathrm{cwe}}$, should be used to determine the initiation of bedload transport. At higher transport stages, Li et al. (1997), following the results of other studies (Smith and McLean, 1977; Wilson, 1988; Wiberg and Harris, 1994; Li, 1994), proposed that the boundary frictional behaviour is controlled mostly by the thickness of the bedload transport layer and that a transport-related bedload shear velocity $u_{*\mathrm{cwb}}$, predicted from the GM86 model using the sum of the

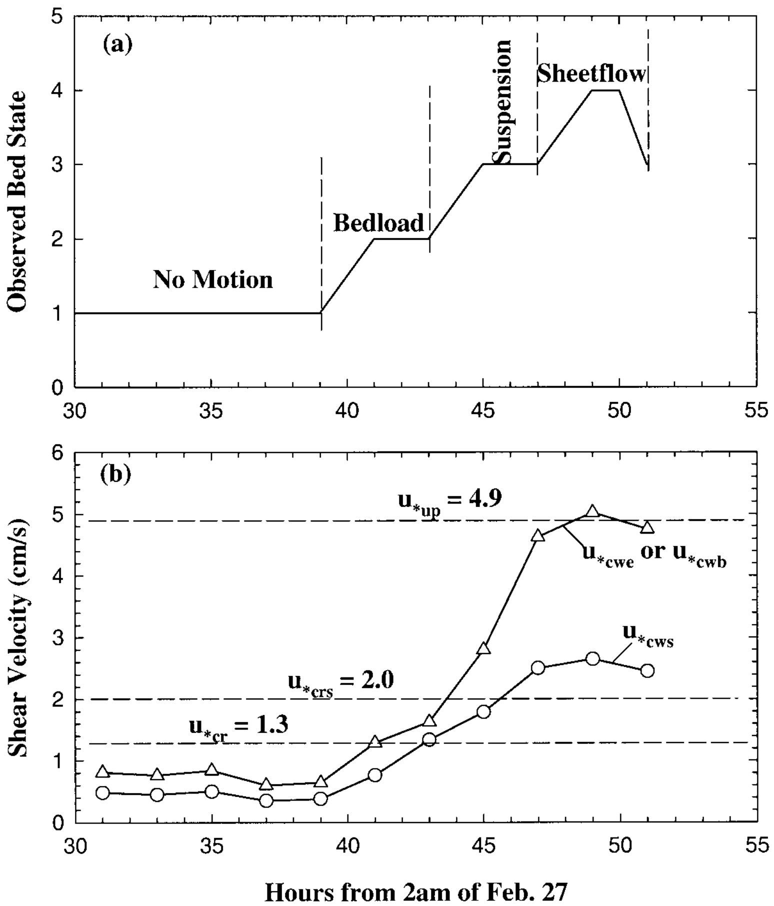

Fig. 5. Comparison between (a) the observed sediment transport modes and (b) various predicted combined shear velocities for the last eleven bursts of the correlated data. The observed bed states in (a) are as defined in Fig. 3. The three dashed lines in (b) indicate the critical shear velocities for bedload ($u_{*\mathrm{cr}}$), suspension ($u_{*\mathrm{crs}}$), and sheet-flow ($u_{*\mathrm{up}}$) transport, respectively. Circles represent the skin-friction combined shear velocity $u_{*\mathrm{cws}}$ and triangles represent ripple-enhanced combined shear velocity $u_{*\mathrm{cwe}}$ (when $u_{*\mathrm{cws}} < u_{*\mathrm{cr}}$) or bedload combined shear velocity $u_{*\mathrm{cwb}}$ (when $u_{*\mathrm{cws}} > u_{*\mathrm{cr}}$).

grain roughness and bedload roughness, should be used to determine the onset of sand suspension and sheet-flow transport. By using these ripple-enhanced and bedload shear velocities, Li et al. (1997) found reasonable agreements between the established critical shear velocities ($u_{*\mathrm{cr}}$, $u_{*\mathrm{crs}}$ and $u_{*\mathrm{up}}$) and the observed onset of bedload, suspension and sheet-flow transport over *medium sand*. In order to extend these findings to *fine sand*, similar exercises were carried out in this study.

The ripple-enhanced shear velocity $u_{*\mathrm{cwe}}$ was calculated according to Nielsen (1986):

$$u_{*\mathrm{cwe}} = \frac{u_{*\mathrm{cws}}}{1 - \pi\eta/\lambda} \tag{2}$$

where η and λ are ripple height and wavelength, respectively. Because of the absence of ripple height measurements in this study, the ripple steepness η/λ needs to be predicted before Eq. 2 can be used. A few recent studies have shown that existing wave-ripple predictors do not work under the combined waves and currents (e.g. Cacchione and Drake, 1990; Osborne and Vincent, 1993; Li et al., 1997). Ripple data collected over medium sand on Sable Island Bank (Li and Amos, 1998) show that the steepness of combined-flow ripples has an average of 0.13. This is significantly smaller than that of wave ripples (around 0.17), but higher than that of current ripples (about 0.1). Therefore the direct use of wave ripple steepness such as predicted, e.g. by the method of Allen (1982), will over-estimate the steepness of the ripples and hence u_{*cwe}. For these reasons, the average ripple steepness of 0.13, estimated by Li et al. (1997) for combined-flow ripples on Sable Island Bank, was used in Eq. 2 to calculate u_{*cwe} for bursts 31 to 41 ($u_{*cws} < u_{*cr}$, sediment transport did not occur). For the remainder of the data bursts in Table 2 ($u_{*cws} > u_{*cr}$, sediment transport occurred), a combined-flow ripple predictor proposed by Li and Amos (1998) was used to predict ripple heights and wavelengths which were then used in Eq. 2 to calculate u_{*cwe}. These calculated values of u_{*cwe} are listed in Table 2 for the selected bursts. The skin-friction combined shear velocity u_{*cws} was greater than the bedload critical shear velocity u_{*cr} for bursts 41 to 51 and general sediment transport occurred in these bursts. By comparing the predicted bedload combined shear velocities with values of established u_{*crs} and u_{*up} for observed suspension and sheet-flow events over medium sand, Li et al. (1997) and Li and Amos (1998) have derived and partially tested the following function of bedload roughness height, k_{bt}, for combined flows:

$$h_{tm} = 2.9D(\theta_{cws} - \theta_{cr})^{0.75} \tag{3a}$$

$$k_{bt} = 180 h_{tm} \tag{3b}$$

where h_{tm} is the thickness scale of the bedload layer, θ_{cws} is the skin-friction combined Shields parameter computed from $\theta_{cws} = \rho u_{*cws}^2/(\rho_s - \rho)gD$, $\theta_{cr} = \rho u_{*cr}^2/(\rho_s - \rho)gD$ is the critical Shields parameter for bedload transport. The bedload roughness height obtained from Eqs. 3a and 3b was added to the grain size roughness height ($2.5D$), then the combined roughness height was used in the GM86 model to predict the bedload shear velocity u_{*cwb}. The predicted values of u_{*cwb} are also listed in Table 2.

The time-series of u_{*cwe} (for bursts in which $u_{*cws} < u_{*cr}$) and u_{*cwb} (for bursts in which $u_{*cws} > u_{*cr}$) are plotted as triangles in Fig. 5b. From bursts 31 to 39, the values of u_{*cwe} are higher than u_{*cws}, but are still less than u_{*cr}. Indeed no sediment transport was observed in these bursts (Fig. 5a). Bedload transport was first observed in burst 41. While u_{*cws} for this burst was 0.76 cm/s and significantly less than $u_{*cr} = 1.3$ cm/s, the ripple-enhanced shear velocity u_{*cwe} was approximately equal to u_{*cr} (Fig. 5b); this indicates that the ripple-enhanced shear velocity predicts well the initiation of bedload transport. Suspension and sheet flow were first observed in bursts 45 and 49, respectively. The predicted bedload shear velocities for these two bursts are, respectively, 2.8 cm/s and 5.02 cm/s. These are comparable with the threshold values (Fig. 5b). This observation demonstrates clearly that the use of the bedload shear velocity can explain the discrepancy between u_{*cws} and the established threshold criterion for sand suspension and sheet-flow transport under combined flow conditions.

4. Summary and conclusions

The correlated video and S4 wave–current meter data recorded the build-up of a moderate storm, during which the significant wave height increased quickly from less than 0.5 m in fairweather condition to >3 m at the peak of the storm. The mean current speed at 50 cm above the seabed increased from less than 0.1 m/s to about 0.25 m/s. As the storm built up, a sequence of bedforms was observed. At the early stages of the storm, relict wave-dominant ripples with worm tubes and animal tracks first changed into irregular, sinuous, asymmetrical current-dominant and intermediate wave–current ripples under bedload transport. These bedforms were followed by regular, nearly straight or sinuous, asymmetrical or slightly asymmetrical wave-dominant ripples under strong sand suspension. At the peak of the storm, the ripples were completely washed out and upper-plane bed sheet flow prevailed. As bed shear stress decreased in the last burst of the correlated data due to the substantial drop of the mean current, the plane bed under the sheet-flow condition changed into lunate megaripples as sediment fell out from suspension. At the transition from suspension to upper-plane bed sheet flow during the storm build-up and also before the sheet flow changed into lunate megaripples during the decay of the storm, the formation of small, asymmetrical, crest-reversing transitory ripples were observed under quasi-sheet-flow condition.

Data from the present and previous studies indicate that when waves and currents are orthogonal or at large angles, independent symmetrical wave ripples and asymmetrical current ripples will co-exist to form cross-pattern ripples. When waves and currents are parallel or at small angles, intermediate combined wave–current ripples will occur. The asymmetrical intermediate wave–current ripples can be differentiated from asymmetrical current or current-dominant ripples by their rounded crests, straighter and more regular forms, and associated bifurcations. Crest-reversing transitory ripples were observed to develop at the transition between sand suspension and upper-plane bed sheet flow. The formation of these ripples is due to the oscillatory motion of the combined flow, the near sheet-flow energetic condition and long wave periods at this stage of the storm process. The small height, strong asymmetry and the associated high-regime flow dynamics of these transitory ripples can be used to distinguish them from the regular lower-regime current ripples.

When ripples are present, the bed shear stress will increase from the ripple trough to crest. The use of the average skin-friction combined shear velocity will underestimate the onset of the bedload transport. The ripple-enhanced skin-friction combined shear velocity must be compared with the critical shear velocity to adequately determine the initiation of bedload transport. This agrees with previous field and laboratory studies (Kapdasli, 1990; Li et al., 1997). For the observed suspension and sheet-flow events, the values of the skin-friction combined shear velocity u_{*cws} were found to be substantially lower than the established critical shear velocities for suspension (u_{*crs}) and sheet-flow (u_{*up}) transport modes. Direct comparisons of u_{*cws} with u_{*crs} and u_{*up} will under-estimate the onset of sediment suspension and sheet-flow transport. At these high transport stages, results from previous studies suggest that the boundary layer dynamics and frictional behaviour of near-bed flow is mostly dependent on the thickness scale of the bedload transport layer. The sum of the grain roughness and the bedload roughness was thus used in this study to obtain a transport-related combined shear velocity u_{*cwb}. When the values of this bedload shear velocity were compared with the conventional critical shear velocities for suspension and sheet-flow transport modes for the observed suspension and sheet-flow events, reasonable agreement was achieved. This, together with similar findings over medium sand sediment from previous studies (Li et al., 1997), indicates that the established critical shear velocities for suspension and sheet-flow transport modes are applicable to combined waves and currents if they are compared against the transport-related bedload shear velocity u_{*cwb}.

Acknowledgements

The authors would like to thank John Zevenhuizen, Bruce Wile and Angus Robertson for instrumentation and field support. Don Clattenburg analysed the grain size. We also appreciate the co-operation of Pan Canadian (formerly LASMO Ltd.) during the field work. David Piper and Bob Taylor critically reviewed the original manuscript of this contribution. We also appreciate the comments from professor Michael Collins and an anonymous journal referee. The funding for this work was provided by the Panel on Energy Research and Development (PERD) of the Federal Government of Canada through Offshore Geotechnics Program 63204. Geological Survey of Canada contribution number 1998118.

References

Allen, J.R.L., 1982. Sedimentary Structures: Their Character and Physical Basis, Vol. 1. Elsevier, Amsterdam, 593 pp.

Amos, C.L., Bowen, A.J., Huntley, D.A., Lewis, C.F.M., 1988. Ripple generation under the combined influences of waves and currents on the Canadian continental shelf. Cont. Shelf Res. 8, 1129–1153.

Amos, C.L., Li, M.Z., Choung, K.-S., 1996. Storm-generated swaley bedding on the outer Scotian Shelf. Geo-Mar. Lett. 16, 85–94.

Bagnold, R.A., 1956. Flow of cohesionless grains in fluids. Philos. Trans. R. Soc. London A 249, 235–297.

Cacchione, D.A., Drake, D.E., 1990. Shelf sediment transport: an overview with applications to the Northern California continental shelf. In: Le Mehaute, B., Hanes, D.M. (Eds.), The Sea, Vol. 9. Wiley-Interscience, New York, pp. 729–773.

Clifton, H.E., 1976. Wave-formed sedimentary structures — a conceptual model. In: Davis, A.R. Jr., Ethington, R.L. (Eds.), Beach and Nearshore Sedimentation. Soc. Econ. Paleontol. Mineral. Spec. Publ. 24, 126–148.

Dingler, J.R., Inman, D.L., 1976. Wave-formed ripples in nearshore sands. In: Proc. 15th Coastal Engineering Conf., ASCE, New York, pp. 2109–2126.

Downing, J.P., 1983. An optical instrument for monitoring suspended particulates in ocean and laboratory. In: Proc. Oceans '83, pp. 199–202.

Grant, W.D., Madsen, O.S., 1982. Moveable bed roughness in unsteady oscillatory flow. J. Geophys. Res. 87, 469–481.

Grant, W.D., Madsen, O.S., 1986. The continental shelf bottom boundary layer. Annu. Rev. Fluid Mech. 18, 265–305.

Greenwood, B., Sherman, D.J., 1986. Hummocky cross-stratification in the surf zone: flow parameters and bedding genesis. Sedimentology 33, 33–45.

Hammond, T.M., Collins, M.B., 1979. On the threshold of transport of sand-sized sediment under the combined influence of unidirectional and oscillatory flow. Sedimentology 26, 795–812.

Harms, J.C., Southard, J.B., Walker, R.G., 1982. Structures and Sequences in Clastic Rocks. Soc. Econ. Paleontol. Mineral., Short Course 9, 249 pp.

Kapdasli, M.S., 1990. Threshold condition of sand particles under codirectional combined wave and current flow. Geo-Mar. Lett. 10, 45–49.

Komar, P.D., Miller, M.C., 1974. Sediment threshold under oscillatory waves. Proc. 14th Conf. Coastal Engineering, ASCE, Copenhagen, pp. 756–775.

Komar, P.D., Miller, M.C., 1975. The initiation of oscillatory ripple marks and the development of plane-bed at high shear stresses under waves. J. Sediment. Petrol. 45, 697–703.

Larsen, L.H., Sternberg, R.W., Shi, N.C., Marsden, M.A.H., Thomas, L., 1981. Field investigations of the threshold of grain motion by ocean waves and currents. Mar. Geol. 42, 105–132.

Li, M.Z., 1994. Direct skin friction measurements and stress partitioning over movable sand ripples. J. Geophys. Res. 99, 791–799.

Li, M.Z., Amos, C.L., 1998. Predicting ripple geometry and bed roughness under combined waves and currents in a continental shelf environment. Cont. Shelf Res. 18, 941–970.

Li, M.Z., Wright, L.D., Amos, C.L., 1996. Predicting ripple roughness and sand resuspension under combined flows in a shoreface environment. Mar. Geol. 30, 139–161.

Li, M.Z., Amos, C.L., Heffler, D.E., 1997. Boundary layer dynamics and sediment transport under storm and non-storm conditions on the Scotian shelf. Mar. Geol. 141, 157–181.

Madsen, O.S., Grant, W.D., 1975. The threshold of sediment movement under oscillatory waves: a discussion. J. Sediment. Petrol. 45, 360–361.

Manohar, M., 1955. Mechanics of bottom sediment movement due to wave action. U.S. Army Corps Engineers, Beach Erosion Board, Tech. Mem. 75, 121 pp.

Miller, M.C., McCave, I.N., Komar, P.D., 1977. Threshold of sediment motion under unidirectional currents. Sedimentology 24, 507–527.

Mobil Oil Canada Ltd., 1983. Venture development project environmental impact statement, vol. IIa, Biophysical assessment. Mobil Oil Canada Ltd., Submitted to Canada Oil and Gas Lands Administration, Ottawa, 415 pp.

Nielsen, P., 1981. Dynamics and geometry of wave-generated ripples. J. Geophys. Res. 86, 6467–6472.

Nielsen, P., 1986. Suspended sediment concentrations under waves. Coastal Eng. 10, 23–31.

Osborne, P.D., Vincent, C.E., 1993. Dynamics of large and small scale bedforms on a macrotidal shoreface under shoaling and breaking waves. Mar. Geol. 115, 207–226.

Smith, J.D., 1977. Modelling of sediment transport on continental shelves. In: Goldberg, E.D. et al. (Eds.), The Sea, Vol. 6. Wiley-Interscience, New York, pp. 539–577.

Smith, J.D., McLean, S.R., 1977. Boundary layer adjustments to bottom topography and suspended sediments. In: Nihoul, J.C.J. (Ed.), Bottom Turbulence. Elsevier, New York, pp. 123–151.

Swift, D.J.P., Figueiredo, A.G., Freeland, G.L., Oertel, G.F., 1983. Hummocky cross-stratification and megaripples: a geological double standard? J. Sediment. Petrol. 53 (4), 1295–1318.

Van Rijn, L.C., Havinga, F.J., 1995. Transport of fine sands by currents and waves, II. J. Waterway, Port, Coastal Ocean Eng. ASCE 121 (2), 123–133.

Van Rijn, L.C., Nieuwjaar, M.W.C., Van der Kaay, T., Nap, E., van Kampen, A., 1993. Transport of fine sands by currents and waves. J. Waterway, Port, Coastal Ocean Eng. ASCE 119 (2), 123–143.

Vincent, C.E., Hanes, D.M., Bowen, A.J., 1991. Acoustic measurements of suspended sand on the shoreface and the control of concentration by bed roughness. Mar. Geol. 96, 1–18.

Wiberg, P.L., Harris, C.K., 1994. Ripple geometry in wave-dominated environments. J. Geophys. Res. 99, 775–789.

Wilson, K.C., 1988. Mobile-bed friction at high shear stress. J. Hydraul. Eng. ASCE 115 (6), 825–830.